Nonadiabatic Simulation of Exciton Dynamics in Organic Semiconductors Using Neural Network-Based Frenkel Hamiltonian and Gradients

Farhad Ghalami, Philipp M. Dohmen, Mila Krämer, Marcus Elstner, and Weiwei Xie*

ABSTRACT: In this study, we present a multiscale method to simulate the propagation of Frenkel singlet excitons in organic semiconductors (OSCs). The approach uses neural network models to train a Frenkel-type Hamiltonian and its gradient, obtained by the long-range correction version of density functional tight-binding with self-consistent charges. Our models accurately predict site energies, excitonic couplings, and corresponding gradients, essential for the nonadiabatic molecular dynamics simulations. Combined with the fewest switches surface hopping algorithm, the method was applied to four representative OSCs: anthracene, pentacene, perylenediimide, and diindenoperylene. The simulated exciton diffusion constants align well with experimental and reported theoretical values and offer valuable insights into exciton dynamics in OSCs.

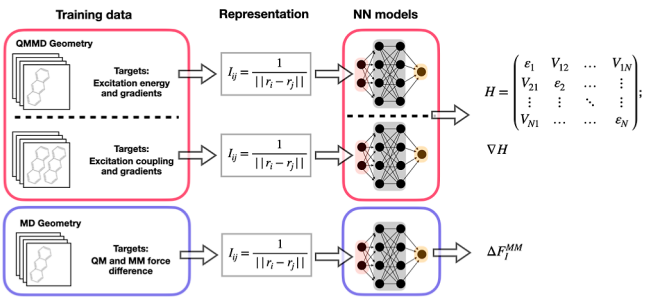

1. INTRODUCTION

Organic semiconductors (OSCs) have garnered significant attention across multiple technological domains in the past decade.[1] They have emerged as essential elements in diverse electronic devices, notably in organic light-emitting diodes for cutting-edge display technologies,[2−4] organic field-effect transistors,[5,6] organic photovoltaic devices,[7−9] and even organic batteries.[10,11]

Exciton transport in bulk organic semiconductors (OSCs) is also important due to its potential impact on the photoelectric efficiency. Fast exciton transport in OSCs results in a longer diffusion length, which can enhance the overall efficiency of the photoelectric processes. The absorption of light generates molecular excitations, manifested as bound electron−hole pairs, known as Frenkel excitons. These excitons induce a manifold of relaxation processes in organic materials. Understanding Frenkel excitons is pivotal for the design and optimization of organic semiconductors. Additionally, beyond their significance in molecular crystals and organic semiconductors, Frenkel excitons have been subjects of study in other systems, including carbon nanotubes[12] and graphene.[13] Overall, they represent a crucial type of excited state in molecular systems, offering a broad spectrum of potential applications in areas such as optoelectronics and energy conversion.[14] However, a significant challenge persists in understanding the correlations between molecular properties, packing, and exciton transport within organic semiconductors. Furthermore, the extensive diversity of available organic compounds makes the pursuit of suitable candidates both time-consuming and financially demanding. In this context, theoretical approaches employing simulation techniques can play a pivotal role by complementing experimental insights or expediting the attainment of similar insights.[15] This enables efficient screening of a vast compound space for promising properties prior to their synthesis.[16] To achieve this goal, the development of rapid and robust methods capable of simulating charge and exciton transfer in large molecular systems, while accurately reproducing experimentally observable quantities such as the exciton diffusion constant, becomes essential.

Within Marcus theory, the propagation of Frenkel excitons can be elucidated through several parameters, including excitation energy, excitonic couplings, and reorganization energy.[17,18] The transfer mechanism is then described as

localized (Frenkel) exciton transferred by thermal activation.[19] However, this method is not applicable to treat the fast exciton transport in OSCs, where the Frenkel exciton is delocalized over a few molecules.

Recently, nonadiabatic molecular dynamics methods (e.g., fewest switches surface hopping (FSSH) and mean-field Ehrenfest) have been used to model charge and exciton transport processes in OSCs,[20−29] which have been rationalized as alternative transport mechanism known as 'transient localization'.[30−35] These methods do not impose any prior assumption on the transport mechanism and thus can go beyond the limits of the traditional Marcus theory. However, the computational cost remains a challenge, as electronic structure calculations are still required to evaluate the charge-/exciton-transfer Hamiltonian at each time step during simulations. In our previous works, we have developed the semiempirical method, LC-TDDFTB,[36−38] to evaluate the exciton coupling and excitation energy for OSCs. While the benchmark results have shown its high accuracy and significant computational time reduction (several order of magnitudes) compared to density functional theory (DFT), it remains impractical for the high-cost nonadiabatic molecular dynamics simulations that necessitate frequent electronic structure calculations (e.g., 10,000 times for 1 ps simulation).

In this work, we extend our multiscale methodology by employing neural network models to simulate the propagation of Frenkel singlet excitons in OSCs. In our prior work,[39] we employed a comparable methodology to simulate charge transfer in OSCs. In the current study, we improved our model by incorporating an additional neural network model. This addition aims at correcting the ground-state forces within the general Amber force field (GAFF), thereby achieving a more accurate reproduction of exciton relaxation. First, we describe the quantum mechanics/molecular mechanics (QM/MM) approach applied in this work, which allows for the seamless integration of neural network potentials. We derive a total energy expression that is integrated into a standard NAMD scheme based on FSSH. The electronic structure of the molecules in the crystal's quantum region is approximated using a fragmentation method. This is further modeled by a Frenkel Hamiltonian, which in turn can be represented through neural network (NN) models. The NN models also cover a correction to the classical MD forces. We apply this methodology to four OSC crystals, anthracene (ANT), pentacene (PEN), perylenediimide (PDI), and diindenoperylene (DIP), to estimate the exciton diffusion constants.

2. METHODS

The applied multiscale methodology is based on a methodology we developed in recent years for the simulation of rapid electron and exciton-transfer processes across various domains, encompassing electron transfer in DNA, photolyase,[40−42] and electron and exciton transfer in organic materials.[19−21,23,39,43−45] It has three major ingredients: (i) it is based on a QM/MM embedding scheme, i.e., only a part of the crystal is treated using quantum mechanics, and the remainder of the system is treated classically. (ii) The electronic excitations are represented by Frenkel Hamiltonian, wherein the Hamiltonian elements are predicted by a NN trained w.r.t. data generated by the semiempirical DFTB method. (iii) The propagation of the exciton is coupled to the nuclear motion using a nonadiabatic molecular dynamics scheme based on Tully's FSSH with corrections for decoherence and trivial crossings.[23] In the following, we shortly describe these components.

2.1. Quantum Mechanics/Molecular Mechanics Scheme. In QM/MM simulations, the system is partitioned into a quantum mechanical region (QM), where the exciton is situated and is governed by the principles of quantum mechanics, and a molecular mechanical region (MM), which represents the surrounding environment and is governed by a classical force field. For the quantum region, we usually consider a linear chain of molecules oriented along one of the crystal axes.[19−21,23,39,43−45] In this work, we use the so-called subtractive QM/MM scheme,[46] where the MM force field covers the whole system including the quantum region leading to the total energy for excitons as[19−21,23,39,45]

$$E^{\mathrm{tot}} = E^{\mathrm{MM}} + \Delta E^{\mathrm{MM}} + \Delta E^{\mathrm{QM}}_{\mathrm{ex}} + \Delta E_{\mathrm{QM/MM}} \tag{1}$$

E_{MM} is the force field energy; in a subtractive QM/MM scheme, the entire system is described by this energy. ΔE_{MM} is a term representing the energy difference between the QM and the MM description of the molecules in the quantum region. $\Delta E^{\mathrm{QM}}_{\mathrm{ex}} = E_{\mathrm{ex}} - E_{\mathrm{ground}}$ is the energy difference of ground and excited states in the QM region described by the QM method. In a mechanical embedding scheme, the electrostatic and van der Waals interactions between the QM and MM regions are already covered by the E^{MM} term, while $\Delta E_{\mathrm{QM/MM}}$ describes the difference of these interactions between excited and ground states, which is small for the systems considered here; therefore, $\Delta E_{\mathrm{QM/MM}}$ is neglected in this work. A comprehensive discussion in this regard is added in Supporting Information Section S5.

Consider now an excitation to a particular excited state, e.g., the first singlet excited state S_1; $\Delta E^{\mathrm{QM}}_{\mathrm{ex}}$ represents the $S_0 \rightarrow S_1$ excitation energy. Nuclear forces can be readily derived by taking the derivatives of eq 1 w.r.t. nuclear coordinates as

$$F^{\mathrm{tot}} = F^{\mathrm{MM}} + \Delta F^{\mathrm{MM}} + \Delta F^{\mathrm{QM}}_{\mathrm{ex}} + \Delta F_{\mathrm{QM/MM}} \tag{2}$$

The 'Δ' forces ΔF^{MM} and $\Delta F^{\mathrm{QM}}_{\mathrm{ex}}$ are just the difference of the forces between MM and QM methods in the ground state and the difference of QM forces in excited and ground states, respectively, which are predicted by NN models in this study. $\Delta F_{\mathrm{QM/MM}}$ is neglected as discussed above.

2.2. Frenkel Hamiltonian. The computation of the excited-state properties of chromophores within condensed phases through QM/MM approaches has now become a standard practice. However, the task of accurately depicting exciton diffusion—where the excitation, potentially delocalized across multiple chromophores, propagates through the system—presents further complexities. This is particularly true for systems like organic semiconductors. Therefore, we need an efficient representation of $\Delta E^{\mathrm{QM}}_{\mathrm{ex}}$. In this work, we focus on singlet exciton transfer within OSC crystal structures; i.e., we consider a single excitonic band which is constituted by localized singlet molecular excitations, described by Frenkel excitonic Hamiltonian.

$$\widehat{H} = \sum_{n} \epsilon_n(t) |\phi_n\rangle\langle\phi_n| + \sum_{n \neq .m} V_{nm}(t) |\phi_n\rangle\langle\phi_m| \tag{3}$$

Here, $|\phi_n\rangle$ represents the state where the excitonic state is localized on molecule n, and the rest of the system is in the ground state. n and m run over all of the molecules in the QM region. The energy of such a state is represented by ϵ_n. V_{nm} denotes the intermolecular exciton coupling between states |

$\phi_n\rangle$ and $|\phi_m\rangle$. The resulting Hamiltonian is an $n \times n$ matrix, with ϵ_n as diagonal and V_{mn} as off-diagonal matrix elements.

Following our previous work, we approximate the couplings using the Coulomb interactions between the transition densities of neighboring pigments.[19] These are then further approximated by Mulliken transition charges Q from single chromophores. Pure Coulomb coupling of the transitions from the ground state (g) to the excited state (e), respectively, on sites n and m involves the summation of the products of the transition charges (Q_{eg}) of atom A in site n and atom B in site m. This can be represented as[47]

$$V_{nm}(\mathrm{eg}, \mathrm{eg}) = \sum_{A\in m} \sum_{B\in n} Q_{eg}^{A} Q_{eg}^{B} \gamma_{AB} \tag{4}$$

The distance dependence is represented by a function γ_{AB}, approximating the two-electron integrals in DFTB; see ref 19 for details. The functional form of γ_{AB} also can be found in Supporting Information Section S3. Using the semiempirical TD-LC-DFTB method instead of ab initio or DFT approaches speeds up the calculations by several orders of magnitude.[19,47] It is noted that, in contrast to ref 19 we now use range-separated functionals with DFTB, i.e., LC-DFTB. This approach has been thoroughly tested w.r.t. various DFT and ab initio methods.[36,38]

2.3. Exciton Propagation. Exciton wave function, $|\psi\rangle$, in the noncovalent solids can be expanded as a linear combination of localized molecular excitations $|\phi_n\rangle$

$$\psi(t) = \sum_n a_n(t) |\phi_n(\mathbf{R}(t))\rangle \tag{5}$$

Inserting this wave function into the time-dependent Schrödinger equation (TDSE), we obtain the time evolution of the wave function for the expansion coefficients as

$$\dot{a}_m = -i \sum_n H_{mn} a_n - \sum_n a_n \langle \phi_m | \dot{\phi}_n \rangle \tag{6}$$

The last term is very small for molecules far apart[19−21,23] and is therefore usually neglected.

To apply Tully's FSSH method, we have to represent the equations of motion in terms of adiabatic states. Diagonalization of the Hamiltonian, eq 3 for any nuclear conformation of the molecules in the QM region leads to the adiabatic eigenstates (stationary) $|\psi_i\rangle$ of the system. Alternative to the expansion in a diabatic basis, eq 5, the exciton wave function can be expanded as a linear combination of adiabatic wave functions, $|\psi_i\rangle$

$$\Psi(t) = \sum_i C_i^{\mathrm{ad}}(t) |\psi_i(\mathbf{R}(t))\rangle \tag{7}$$

Inserting this wave function into TDSE, we obtain the time evolution of the wave function from the expansion coefficients as

$$i\hbar \dot{C}_i^{\mathrm{ad}} = C_i^{\mathrm{ad}} E_i^{\mathrm{ad}} - i\hbar \sum_j C_j^{\mathrm{ad}} d_{ij}^{\mathrm{ad}} \tag{8}$$

where E_i^{ad} is the adiabatic potential energy of the adiabatic state $|\psi_n\rangle$ and can be obtained from the diagonalization of the Hamiltonian matrix H_{mn} as

$$\mathbf{H}^{\mathrm{ad}} = \mathbf{U}^{\dagger} \mathrm{H} \mathrm{U} \tag{9}$$

d_{ij}^{ad} are nonadiabatic coupling elements (NACEs) which are derived using the chain rule as

$$d_{ij}^{\mathrm{ad}} = \langle \psi_i | \frac{\mathrm{d}\psi_j}{\mathrm{d}t} \rangle \tag{10}$$

where bold $\mathbf{d}_{ij}^{\mathrm{ad}}$ in eq 10 denotes the nonadiabatic coupling vector (NACV) which is given as[23,45,48,49]

$$\mathbf{d}_{ij}^{ad} \approx \frac{[\mathbf{U}^{\dagger} \nabla \mathrm{H} \mathrm{U}]}{E_i^{\mathrm{ad}} - E_j^{\mathrm{ad}}} \tag{11}$$

Classical trajectories evolve on a single adiabatic energy surface E_i^{ad} in the QM region, based on Newton's second law. Considering the subtractive QM/MM scheme, we write the forces from eq 2 (neglecting $\Delta F_{\mathrm{QM/MM}}$)

$$m_{\mathrm{I}} \ddot{\mathbf{R}}_{\mathrm{I}} = F_{\mathrm{I}}^{\mathrm{MM}} + \Delta F_{\mathrm{I}}^{\mathrm{MM}} + \nabla_{\mathrm{I}} E_0 - \nabla_{\mathrm{I}} E_1 \tag{12}$$

where m_{I} and $\mathbf{R}_{\mathrm{I}}$ are the mass and position of atom I, respectively, $F_{\mathrm{I}}^{\mathrm{MM}}$ and $\Delta F_{\mathrm{I}}^{\mathrm{MM}}$ are the derivatives of the respective energies w.r.t. the nuclear coordinates, and E_0 and E_1 are the ground-state and first excited-state energies of the single molecule of the crystal. We have thereby expressed

$$\Delta F_{\mathrm{ex}}^{\mathrm{QM}} = \nabla_{\mathrm{I}} E_0 - \nabla_{\mathrm{I}} E_1 \tag{13}$$

as the difference between excited- and ground-state forces. Eqs 12 and 6 are solved iteratively, thereby simultaneously propagating the electronic and nuclear degrees of freedom.

The hopping from state $|\psi_i\rangle$ to state $|\psi_j\rangle$ is determined by the comparison of the transition probabilities $P_{i\to j}$, calculated based on the FSSH algorithm and corrections for decoherence and trivial crossings. Details are given in our previous works.[19,23,45]

In maintaining the principle of total energy conservation across each trajectory, it becomes necessary to adjust the nuclear momenta during a transition, commonly known as a 'hop'. Conventionally, this is accomplished by scaling the nuclear velocities or momenta along the direction of the nonadiabatic coupling vector (NACV), eq 11. This implies the need for regular computation of NACVs between the active adiabatic state and all others at every nuclear time step.[23,49]

In this work, the NACVs are computed according to eq 11 based on the NN-predicted Hamiltonian and its gradients. This novel approach eliminates the need for the traditional numerical calculation of nonadiabatic coupling vectors, significantly enhancing the computational speed and efficiency.

An alternative method, however, involves adjusting the hopping probability, by applying a Boltzmann factor, $\exp\left(-\frac{H_j^{\mathrm{ad}} - H_i^{\mathrm{ad}}}{kT}\right)$. This adjustment is made while leaving the velocities unchanged. This alternative method is termed the Boltzmann-corrected fewest switches surface hopping (BC-FSSH). One of its primary advantages lies in bypassing the computationally intensive recalculations of NACVs, while still producing good results compared to isotropic rescaling.[45]

After a hop occurs, the molecular fragments occupied by the exciton respond to the changed electronic state by relaxing their geometry, resulting in a decrease in their energies, i.e., the forces on the current occupied fragment change from ground- to excited-state forces, following the new forces leading to a lowering of the energy of this site, i.e., ϵ_n decreases during this relaxation. Using the FSSH or BC-FSSH approach, relaxation is explicitly incorporated through molecular dynamics. We refer to this method as explicit relaxation (ER).

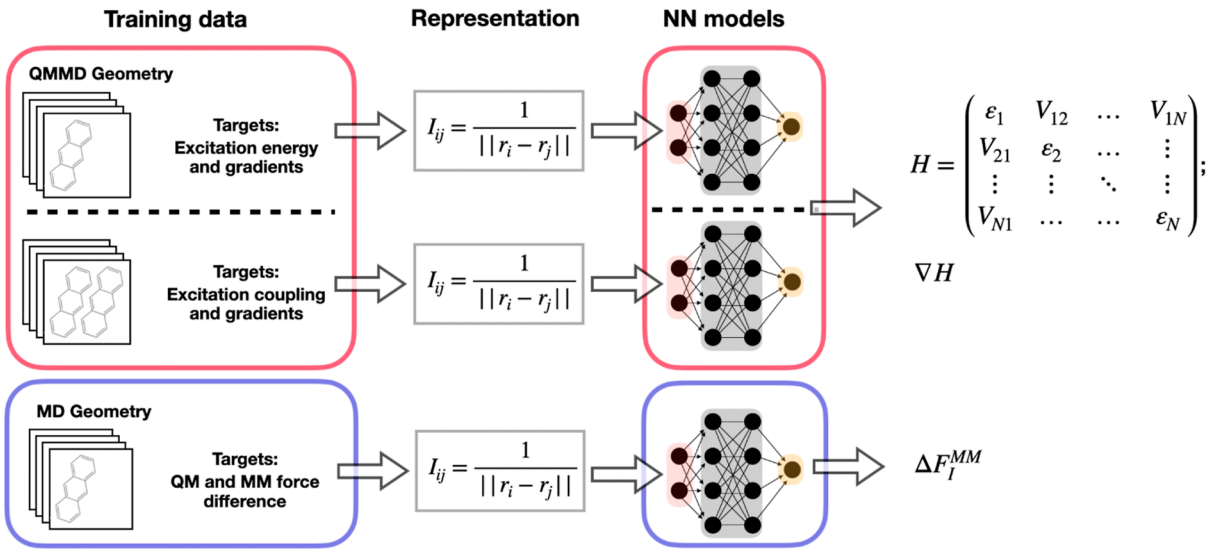

Figure 1. Illustration of the NN models. Top row: site energies and their corresponding gradients. Middle row: exciton coupling and gradients. Bottom row: QM force field correction.

In the Marcus theory, this effect is captured by the reorganization energy λ. In our previous work, we have introduced a very effective approximation, called implicit relaxation (IR). Using this method, the explicit effect of relaxation is replaced by an effective contribution to the Hamiltonian matrix elements in eq 6 (neglecting the last term) as

$$\dot{a}_m = -i\sum_n a_n(H_{mn} - \lambda a_n \delta_{mn}) \tag{14}$$

The energy of the sites is lowered by the reorganization energy λ weighted by their population $|a_n|^2$. λ is a precalculated parameter which usually takes the value of reorganization energy. The advantage of the IR method is that it avoids the computation of QM forces, and the whole system dynamics is driven by the MM-forces F_{MM} alone. No difference forces have to be learned, which simplifies the training process of the model significantly. Since for some systems the reorganization energies sensitively depend on the quantum method applied, this method also allows for a quick estimate of the nuclear relaxation effects on the propagation dynamics, as discussed in detail in ref 45 for charge transfer. Furthermore, it facilitates the integration of reorganization energy values derived from more precise computational methods like DFT, rather than relying solely on (LC)DFTB. This enhancement is crucial for conducting accurate charge-transfer simulations.[39] This method will be abbreviated by BC-FSSH-IR. In the following, we will apply both, the FSSH (ER) method computing NACVs and using ER, as well as the BC-FSSH-IR method.

2.3.1. Hamiltonian Prediction Using Machine Learning Methods. Neural networks are highly versatile statistical models that are widely used to address complex regression or classification problems. They consist of interconnected layers of neurons that process the input data. Each neuron performs a linear combination of inputs, incorporating adjustable weights. These linear combinations are then passed through nonlinear activation functions, enabling the network to accurately approximate intricate functions. In our application, we have employed the neural network architecture previously introduced by Li et al.[50] This architecture was originally designed for predicting energies and gradients related to the electronic states of small organic molecules. The details of the neural network architecture can be found in ref 50. Our training process involved three distinct types of models, each assigned to predict specific target properties. This decision was driven by variations in the input dimensionality among these properties.

One model was exclusively trained to predict site energies and their corresponding gradients (Figure 1 top row).[48] A second model was dedicated to predicting couplings and their gradients (eq 4). The third model was designed to correct the classical force field acting on the molecules within the QM zone, enabling the force field to accurately reproduce the ground-state LC-DFTB2 forces (Figure 1 bottom row), i.e., ΔF^{MM} in eq 2 is represented by this NN. This model is essential for replicating the LC-DFTB2 reorganization accurately in our nonadiabatic molecular dynamics simulations of exciton transfer (Section S4).

2.4. Simulation Details. In this work, we use the semiempirical TD-LC-DFTB2[51] method with the OB2 parameters[52] to generate the training data. TD-LC-DFTB2 uses the usual DFTB approximation combined with a range-separated functional. The application of TD-LC-DFTB2 for our problem is possible, since (i) the excitation energies,[51] (ii) the excited-state forces,[37] and (iii) the exciton couplings[36,38] have been shown to be computed with very good accuracy compared to range-separated time-dependent density functional theory (TD-DFT) methods. We report further testing for the molecules considered in this work in the following sections.

2.4.1. Excitation Energies and Excited-State Forces. To establish a suitable theoretical framework for assessing the diagonal elements of the excitonic Hamiltonian (site energy) described in eq 3, a comprehensive comparative analysis was conducted. The TD-LC-DFTB2 method was subjected to rigorous testing against TD-DFT, employing long-range functionals such as ωB97XD and CAM-B3LYP. The primary objective was to compute the vertical excitation energies and oscillator strengths of the initial singlet excitation within ANT, PEN, PDI, and DIP, as tabulated in Table 1. All TD-DFT calculations were performed by Gaussian16 software pack-

age,[53] and TD-LC-DFTB2 calculations are done using DFTB + software.[54]

Table 1. Vertical Excitation Energies of the First Two Excited States [eV] and the Corresponding Oscillator Strength (in Parentheses) Calculated by TD-LC-DFTB2 and TD-DFT Using Long-Range Functionals ωB97XD and CAM-B3LYP with 6-31G(p, d) Level of Theory

		CAM-B3LYP	ωB97XD	LC-DFTB2
ANT	S_1	3.661 (0.088)	3.685 (0.090)	3.374 (0.090)
	S_2	4.180 (0.004)	4.190 (0.004)	3.898 (0.000)
PEN	S_1	2.355 (0.075)	2.416 (0.081)	2.322 (0.090)
	S_2	3.492 (0.027)	3.525 (0.026)	3.276 (0.000)
PDI	S_1	2.845 (0.765)	2.877 (0.771)	2.715 (0.681)
	S_2	3.771 (0.000)	3.796 (0.000)	3.209 (0.000)
DIP	S_1	2.794 (0.954)	2.831 (0.966)	2.623 (0.906)
	S_2	2.978 (0.000)	3.053 (0.000)	2.768 (0.000)

The molecular geometries were optimized with the respective DFT and LC-DFTB2 methods. We applied ωB97XD and CAM-B3LYP functionals at the 6-31G(d,p) level of theory since they are frequently used for the organic molecules. The LC-DFTB2 calculation adhered to the SCC convergence criterion set at 1×10^{-8}. The parameter defining range separation was set at $\omega = 0.3/a_0$, accompanied by the implementation of a threshold screening method set at 1×10^{-16}, as detailed in ref51. In the LC-DFTB2 method, the conjugate gradient algorithm set for force convergence at its default value was employed for this purpose.

Subsequently, the computation of singlet vertical excitations and oscillator strengths was carried out for the optimized geometries using the corresponding specified level of theory in both the DFT and LC-DFTB2 methods. As a result, we find that LC-DFTB2 is capable to provide a correct description of these properties for the organic molecules studied here, which is in line with the previous tests.[36,37,51,55] The gradient of the site energies, i.e., the difference force ΔF_{ex}^{QM} in eq 13, where E_i is the first excited-state energy and E_0 is the ground-state energy of the monomer in a vacuum, is calculated with the LC-DFTB2 method.

2.4.2. Exciton Coupling. The matrix elements of the excitonic Hamiltonian eq 3 were computed using TD-LC-DFTB2 employing Mulliken transition charges of monomers as delineated in eq 4. This calculation specifically focused on the first singlet excitation, maintaining an SCC convergence criterion set at 1×10^{-8} electrons. The range separation parameter was fixed at $\omega = 0.3/a_0$, accompanied by the application of a threshold screening method set at 1×10^{-16}.

The TD-LC-DFTB2 Coulomb couplings were compared with those obtained from TD-DFT at the ωB97XD level and CAM-B3LYP at the 6-31G(p,d) level of theory employing the excitation energy-transfer (EET) analysis method incorporated in Gaussian 16.[56] The results are presented in Table S1. Additionally, we evaluated the adequacy of Coulomb couplings by comparison with supermolecular couplings, computed through a two-state model Hamiltonian. This model obtained coupled states from the monomer perspectives, with further details provided in the Supporting Information Section S1.

These tests indicate that the Coulomb approximation adequately represents the excitonic couplings in these materials, which is in agreement with our prior research on other materials.[36,38] Specifically, the exchange contributions of the exciton coupling in the investigated materials appear to be negligible, allowing for the total exciton coupling to be expressed primarily through Coulomb interactions of the transition charges.

We also test an additional approximation where atomic transition charges (ATCs) are assumed to be constant during MD simulations, as previously applied in ref 26. This approach involves computing the ATC for a reference monomer and utilizing them for all conformations throughout the MD simulation. Termed TrMull coupling in this context, this method offers two notable advantages. First, it reduces the computation time, as the ATC remains constant throughout the simulation. Second, by assuming the constancy of ATC, the coupling depends solely on γ_{AB}, eq 4, facilitating the analytical calculation of the coupling gradients needed for obtaining nonadiabatic vector coupling as illustrated in eq 11.

2.4.3. Training of Machine Learning Models. All three NN models as described above (Figure 1) take atomic coordinates as inputs from which inverse interatomic distances are computed. This representation, the so-called Coulomb matrix, remains invariant under translation and rotation.

One benefit of this method is that, upon the neural network's prediction of the Hamiltonian and its gradient, we can promptly compute the nonadiabatic vector couplings using eq 11. This streamlines the process significantly, eliminating the necessity for numerically calculating the nonadiabatic coupling vectors, thereby accelerating the overall calculations.

The neural network's trainable component is a multilayer dense feed-forward neural network using the SELU activation function.[57] We conducted the model training using the pyNNsMD package[50] in combination with TensorFlow 2.3[58] and the Keras API.[59] Weight optimization was accomplished through the Adam optimizer,[60] and the loss was measured using mean-squared error. Data for training and validation were split in a 9:1 ratio, enabling us to monitor the validation loss of each epoch and implement early stopping if improvement stagnated for more than 100 epochs. A notable aspect of our approach is that feature calculation and scaling were seamlessly integrated into the neural network architecture. This streamlined the model implementation process, making it more efficient for predictive tasks. Since both site energy/coupling and their gradients are trained simultaneously, the loss function considered both the network's predictions and gradients concerning input coordinates. The relative weights assigned to these components in the loss function were treated as hyperparameters. To find the optimal combinations of these hyperparameters, we utilized the Hyperband algorithm,[61] an efficient and automated approach.

The first model's training data were based on excitation energies of single-molecule structures sampled from ground- and first excited-state LC-DFTB2/MD simulations and the gradient of the site energies which is calculated using eq 13.

The second model was trained to predict the exciton couplings and their gradients. Its training data were obtained from the Coulomb contribution of exciton coupling in dimer structures, sampled from the ground- and first excited-state LC-DFTB2/MD simulations in various crystallographic directions of the corresponding crystals (Figure 1 middle row). The gradient of the Coulomb coupling eq 4 is calculated by considering constant ATCs. In this manner, V_{nm} depends only on γ_{AB} which is in turn a function of distance.

The training data for the third model, which covers the difference of energy and forces between the QM and MM

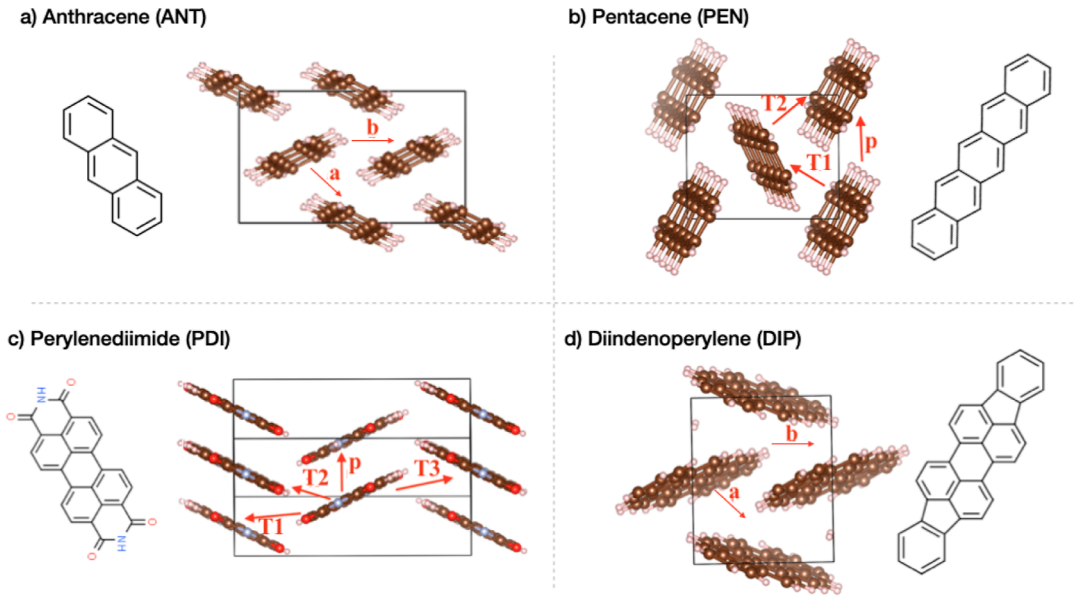

Figure 2. Illustration of (a) ANT, (b) PEN, (c) PDI, and (d) DIP crystals.

levels, was derived from the difference between the LC-DFTB2 ground-state forces and GAFF forces acting on single-molecule structures sampled from classical MD simulations.

It is worth to notice that for both the FSSH-ER and BC-FSSH-IR methods, we have used the same NN models which are simultaneously trained on site energy/coupling and its derivatives, but for the BC-FSSH-IR method, we do not use the gradients.

2.4.4. Sampling and Training Data. To generate the training data required for fitting our neural network (NN) models, we expanded the simulation box of each system by (20 × 5 × 5), based on the unit cell's expansion in various crystallographic directions (see Figure 2).

The force-field parameters were sourced from the GAFF,[62,63] and atomic charges were determined using the restrained electrostatic potential fitting procedure (RESP)[64,65] at the HF/6-31G(p,d) level of theory using Gaussian 16 software.[53] After energy minimization, the initial structures underwent equilibration for 1 ns at 500 K in the NVT ensemble, employing the Nosé−Hoover thermostat.[66] This elevated temperature was selected to increase the exploration of conformational space.

For the purpose of sampling geometries corresponding to both the ground and excited states, QM/MM simulations were performed over a duration of 100 ps. Within each simulation, a molecule was randomly designated for the quantum mechanics (QM) segment, while the remainder of the system was treated using MM. These QM/MM simulations were executed for the ground state and the first excited state of the molecules, employing the long-range-corrected density functional tight-binding method (LC-DFTB2) for the quantum mechanical calculations. Monomer and dimer coordinates from various regions of the crystals were sampled every 100 fs. The local version of GROMACS 5.0.4[67] was used for the molecular dynamics simulations.

For site energy training data, 20,000 single-molecule geometries were sampled from ground-state and first excited-state LC-DFTB2/MD simulations at a 1:1 ratio. The vertical excitations of these sampled structures were calculated by using TD-LC-DFTB2/OB2, with the range-separation parameter ω set to $\omega = 0.3/a_0$. The distribution of the site energies is shown in the Supporting Information Figure S5. The gradients of the site energies were computed using eq 13.

To obtain training data sets for exciton coupling (V_{ij}), 20,000 dimer geometries were sampled from the LC-DFTB2/MM ground- and first excited-state simulations, also at a 1:1 ratio, for each OSC. In these simulations, one monomer resided in the QM zone, while the other was subjected to the classical force field. The distribution of the exciton coupling in different crystallographic directions of the studied systems is depicted in Supporting Information Figure S6. This study considered only the Coulomb contribution to exciton coupling, although it is worth noting that our approach allows for the consideration of other contributions, such as charge-transfer contributions. The calculation of the Coulomb coupling and their gradients within the context of LC-DFTB2 is detailed in ref 19.

Additionally, to generate training data for correcting classical forces, 20,000 monomer geometries from various parts of the crystals were sampled from the MD simulation every 100 ps. The energy difference between GAFF and ground-state LC-DFTB2 forces was computed, and the model was trained based on these differences. The distribution of the training data for the NN models is presented in the Supporting Information.

2.4.5. Exciton Propagation. To simulate exciton transfer utilizing the FSSH algorithm integrated into the local version of GROMACS 4.6 by Abraham et al.,[67] distinct crystals of ANT (20 × 30 × 4), PEN (20 × 20 × 4), PDI (40 × 30 × 4), and DIP (5 × 35 × 4) were generated based on their experimentally determined unit cells. Following equilibration at 300 K using GAFF and a Nosé−Hoover thermostat in an NVT ensemble, the initial structures of the crystals were sampled every 10 ps for subsequent exciton-transfer simulations.

The quantum mechanical (QM) zone was chosen as one-dimensional chains of molecules positioned along the respective directions in the central regions of each crystal. For the ANT crystal, the zones were aligned along the *a*-direction with a chain length of 10 molecules and along the *b*-direction with a length of 15 molecules. In the case of the PEN

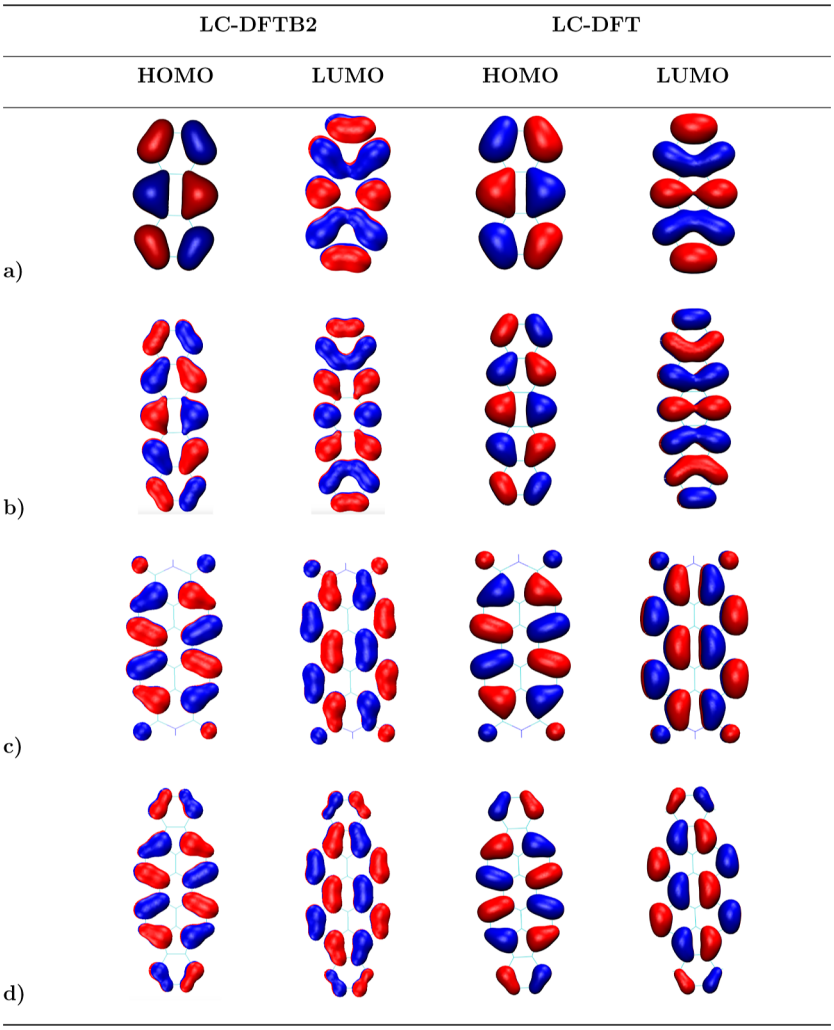

Figure 3. HOMO/LUMO orbitals calculated via LC-DFTB2 and LC-DFT/ωB79 with the def2-TZVP basis set: (a) ANT, (b) PEN, (c) PDI, and (d) DIP.

crystal, the chains were arranged along the p-direction, t_1-direction, and t_2-direction, each extending to 15 molecules. For the PDI crystal, the zones were established along four different directions: the p-direction with 30 molecules and the t_1, t_2, and t_3 directions, each with a length of 18 molecules. Lastly, in the case of DIP, 26 molecules were selected from the b-direction as the QM zone.

The initial localization of the exciton wave function was set on the first molecule of the chain. Our simulations utilized a time step of 0.100 fs for nuclear propagation, while the time-dependent Schrödinger equation (TDSE) was numerically integrated using the fourth-order Runge−Kutta algorithm with an integration time step of 0.010 fs. The mean-squared displacement (MSD) was computed by averaging its values over 500 trajectories, each simulated for 1 ps.

The diffusion constant of the exciton was derived from the MSD using eq 15. The average MSD of the exciton wave function was obtained from 500 trajectories for each system, following which the diffusion constant (D) was calculated using the equation

$$D = \frac{1}{2n}\lim_{t\to\infty}\frac{\mathrm{dMSD}(t)}{\mathrm{d}t}.$$

$$\mathrm{MSD}(t) = \frac{1}{N_{\mathrm{traj}}}\sum_{l}^{N_{\mathrm{traj}}}\sum_{\mathrm{A}}(x_{\mathrm{A}}^{(l)}(t) - x_0^{(l)})^2 P_{\mathrm{A}}^{(l)}(t), \tag{15}$$

where 'n' represents the dimensionality set to 1 in our calculations. Here, $x_{\mathrm{A}}(t)^{(l)}$ and $P_{\mathrm{A}}(t)^{(l)}$ denote the center of mass of molecule A and the corresponding exciton occupation along trajectory 'l', respectively, and $x_0^{(l)}$ signifies the exciton center at t = 0. The inverse participation ratio (IPR), defined by eq 16, elucidates the degree of exciton wave function delocalization across multiple sites

$$\mathrm{IPR} = \frac{1}{N_{\mathrm{traj}}}\sum_{l}^{N_{\mathrm{traj}}}\frac{1}{\sum_k |u_{jk}^{(l)}|^4} \tag{16}$$

3. RESULTS AND DISCUSSION

In this work, we train the neural network models for Frenkel Hamiltonian elements together with its gradients using the training data calculated by LC-DFT B2/OB2. This is possible, since all relevant parameters, i.e., excitation energies, exciton couplings, and reorganization energies, are well reproduced by

LC-DFTB2, as will be shown in the following sections. The neural network will then be used to propagate the excitons using the multiscale approach described above.

3.1. Vertical Excitation Energies. LC-DFTB2 has already been benchmarked for excitation energies with very good agreement with LC-DFT approaches.[36,37,51,55] Here, we want to validate these findings for the specific molecules of interest in the present work. Table 1 shows the excitation energies and oscillator strengths of vertical excitations in the gas phase computed by LC-DFTB2 in comparison with two range-separated DFT methods, CAM-B3LYP and ωB97XD, which have been shown to provide an accurate description of valence and charge-transfer excitations.[68] Both TD-LC-DFTB2 excitation energies and oscillator strengths are in good agreement with the LC-DFT approaches.

The first transition ($S_0 - S_1$) in all four molecules is dominated by a HOMO to LUMO transition, and second excited states (S_2) are, except for DIP, separated by at least 0.5 eV from the first excited state. In DIP, however, the oscillator strength for the second transition ($S_0 - S_2$) is zero, which indicates it to be a dark state. Singlet transition with the lowest energy (S_1) and nonzero oscillator strength f are therefore considered in the following to model Frenkel excitons. Figure 3 illustrates the shape of the HOMO/LUMO orbitals of ANT, PEN, PDI, and DIP, calculated via LC-DFTB2 and LC-DFT with the ωB97XD functional and def2-TZVP as the basis set. Results show that LC-DFTB2 reproduces the electron densities as well as LC-DFT.

3.2. Exciton Coupling. LC-DFTB2 exciton couplings have been thoroughly benchmarked recently for biological and organic molecules,[36,38] showing that LC-DFTB2 couplings match the accuracy of LC-DFT methods quite well. For the molecules of interest in this work, we extend these tests for dimers as extracted from the crystal structures (using the corresponding cif files). We compare TD-LC-DFTB2 Coulomb couplings with those from ωB97XD/6-31G(p,d) and CAM-B3LYP/6-31G(p,d) using the EET method (EET) implemented in Gaussian 16,[53] as shown in Table 2. The good agreement of the LC-DFT methods among themselves and with LC-DFTB2 indicates that LC-DFTB2 using the Coulomb approximation can be employed to generate the training data for the neural network used for exciton propagation. Supermolecule couplings have also been compared to Coulomb couplings, indicating that the exchange contribution of the exciton coupling in these materials is negligible, and the accuracy of the Coulomb coupling is sufficient even for more densely packed organic materials like anthracene.[19,38] The details of the supermolecule coupling calculations are outlined in Supporting Information Table S1. We also investigated the distance dependency of the Coulomb couplings, which show a rapid decay (Supporting Information Figure S1). This justifies to limit the training of the NN models to nearest-neighbor interactions.

Table 2. Coulomb Coupling of Dimers [meV] in Different Crystallographic Directions Calculated by TD-LC-DFTB2 and TD-DFT Using Long-Range Functionals ωB97XD and CAM-B3LYP with 6-31G(p,d) Level of Theory

	dir.	CAM-B3LYP	ωB97XD	LC-DFTB2
ANT	a	1	1	5
	b	−25	−25	−26
PEN	p	−22	−23	−26
	t_1	−6	−6	−10
	t_2	−5	−5	−8
PDI	p	87	86	80
	t_1	−17	−16	−13
	t_2	−13	−13	−12
	t_3	10	10	9
DIP	a	−85	−85	−85
	b	57	57	59

Figure 4 presents a direct comparison between the TrMull and Coulomb couplings derived from 20,000 sampled geometries at 100 ps intervals during the MD simulations of the respective crystals. This sampling technique aligns with the method outlined in the methodology section. The mean values of TrMull and Coulomb couplings closely correspond across all cases. This indicates that utilizing TrMull coupling as an alternative to Coulomb coupling could be a feasible approximation. Noteworthy differences arise in the standard deviations of these couplings. Specifically, the standard deviation of the TrMull couplings tends to be lower compared to that of the Coulomb couplings which implies that fluctuations in the atomic transition charges (ATQs) during simulations contribute to a marginally wider spread in the calculated Coulomb couplings.

3.3. Exciton Relaxation. Exciton−phonon coupling and molecular relaxation in the excited state are essential phenomena affecting the energy transport in organic semiconductors. Therefore, an accurate estimation of exciton−phonon coupling is important in exciton dynamics simulations. In the Marcus theory, this is represented as the reorganization energy λ and is a crucial factor, since it appears in the exponent, the coupling of which only appears as a prefactor in the rate equation. In particular, the relation of coupling to reorganization energy determines the mechanism of transport, featuring the transition from band-like to hopping transport for λ/J. Comparably large values of relaxation energies can cause the transport to become incoherent.[19]

In the Marcus theory, this property is included via a parameter, while in the nonadiabatic simulations, it sensitively depends on the structural changes upon (de) excitation, and a correct description can be highly method-dependent. Alternatively, our formalism also allows to include this as a parameter, which we call 'IR'.[45]

Table 3 shows the computed reorganization energy of a single molecule in the gas phase using LC-DFTB2 and LC-DFT methods through a four-point approach outlined in Supporting Information Section S4. A comparison of these results with the available reference values obtained via the spin component scaling second-order approximate coupled cluster singles and doubles (SCS-CC2) method reveals an overestimation by the LC-DFT method in contrast to SCS-CC2. Furthermore, employing larger basis sets would yield even higher reorganization energy values, as elucidated in Supporting Information Table S2.

Table 3 suggests that LC-DFTB2 is able to predict exciton reorganization energies quite accurately. A comprehensive benchmark study on this matter is detailed in the work by Sokolov et al.[37] This justifies the use of ER based on LC-DFTB2 forces. Note that this is not necessarily the case; e.g., for electron transfer, large deviations depending on the DFT functional have been reported.[39]

3.4. Neural Network Model Training and Validation. As detailed in Training of Machine Learning Models, three

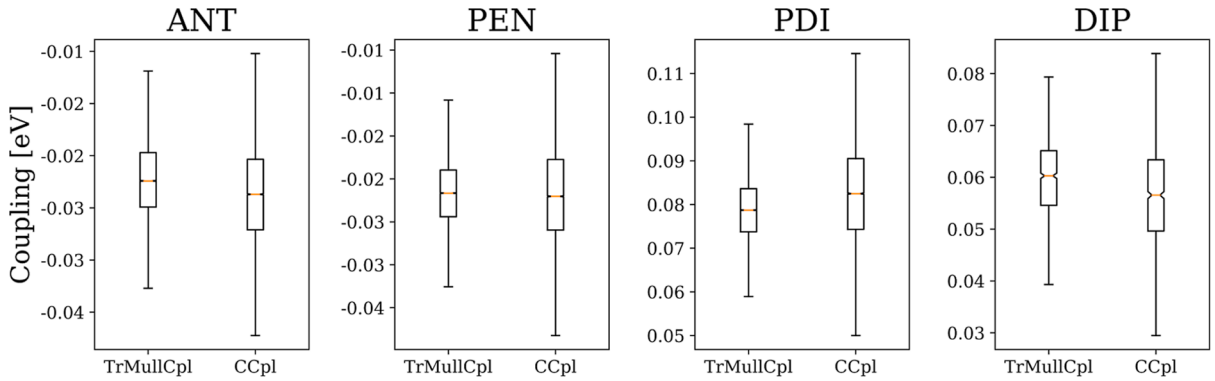

Figure 4. Comparison of TrMull and Coulomb couplings using TD-LC-DFTB2 for sampled structures of ANT, PEN, PDI, and DIP crystals.

Table 3. Comparison of the Reorganization Energy [meV] Calculated from LC-DFTB2 and DFT Using Range-Separated Functionals with 6-31G(p,d) Level of Theory, with the Available Reference Values Calculated from the SCS-CC2 Method

	LC-DFTB2	ωB97XD	CAM-B3LYP	SCS-CC2/cc-pVDZ
ANT	494	562	574	530[69]
PEN	329	420	422	
PDI	367	405	388	
DIP	378	428	412	361[70]

separate neural network models are used in the present study. The first computes the first singlet excitation energies and their gradients based on the monomer structures. The second model predicts the exciton couplings together with the corresponding gradients based on the coordinates of dimers. It is trained on the TD-LC-DFTB2 TrMull coupling, for which derivatives can be computed analytically.[26] The third neural network is trained to capture the difference between the GAFF and the ground-state LC-DFTB2 forces to correct the classical forces so that the average relaxation of the sites would be equal to the reorganization energy of the single molecule calculated via four-point approach using the LC-DFTB2 method.

As the gradients obtained from the model will be converted to forces applied to the system, it is especially important for force predictions to be as reliable as possible. Due to the feedback of the forces to the geometries, a bad force prediction can push the atoms into conformations that are out of the area of the PES sampled during training.

The results of the neural network model fitting are shown in Supporting Information Tables S5−S7. All trained models converged well within 1000 epochs. Site energies and couplings for all the cases were predicted accurately, with models giving low mean absolute error compared to the mean value of the reference sets. The high value of R^2-scores (0.99) indicates that the models are sufficiently trained. The R^2-scores of some of the NN models trained over TrMull coupling slightly diverge from 0.99, Table S6, which primarily originates from the fact that TrMull coupling does not incorporate the geometry-dependent variability of ATCs. As a consequence, the NN model may occasionally misestimate gradient values, particularly when predicting properties of certain dimer configurations where short-range interactions play a significant role. The scattering plots of the ANT site energy and TrMull coupling of the ANT *b*-direction, together with their gradients, illustrated in Figures 5 and 6 respectively, show the absence of the severe outliers in the NN models.

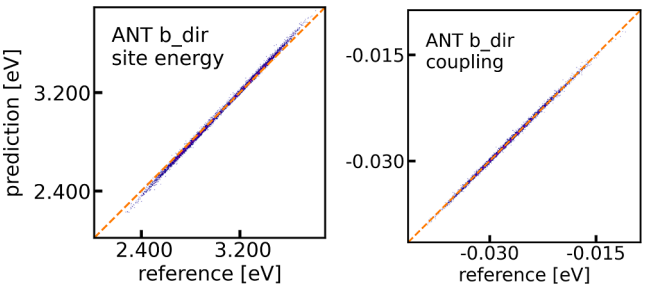

Figure 5. Scattering plots of the NN-predicted excitonic site energy and TrMull coupling of the ANT *b*-direction.

Table 4 presents a comprehensive comparison between neural network models and LC-DFTB2 results regarding the exciton coupling prediction. The results illustrate the neural network models' remarkable capacity to accurately predict coupling values across all scenarios. Furthermore, our neural network models demonstrate a commendable proficiency in predicting the critical parameter of reorganization energy, pivotal for wave function propagation.

To more closely examine the accuracy of the model predictions in relation to the transfer simulation, we calculated and compared the changes in site energy and coupling predictions over the course of the simulation time with benchmark values. For this purpose, benchmark values were determined using LC-DFTB2 across 100 ps simulation trajectories (under the ER scheme) for random molecules in the $\pi-\pi$ stack direction, and first neighbor pairs are considered in the studied crystals (Figures 7 and 8. The site energy predictions throughout the simulation time are consistent. They accurately reproduce the reference values with only minor differences from the reference values, as shown in Figure 7. Exciton coupling prediction also accurately matches the reference values. The large deviation is found for PDI. It is worth to notice that we used a molecular representation which allows to include both inter- and intramolecular atomic distances. This approach therefore also captures rapid oscillations due to bond stretching and internal molecular shifts (Supporting Information Figure S7).

Interestingly, excitonic couplings generally exhibit minor fluctuations when contrasted with electronic coupling. This behavior stems from the moderately affected nature of excitonic couplings amidst geometric alterations induced by lattice vibrations owing to their Coulombic and long-range attributes (r^{-3}). It is noteworthy that, within the hopping regime characterized by formidable barriers, coupling fluctua-

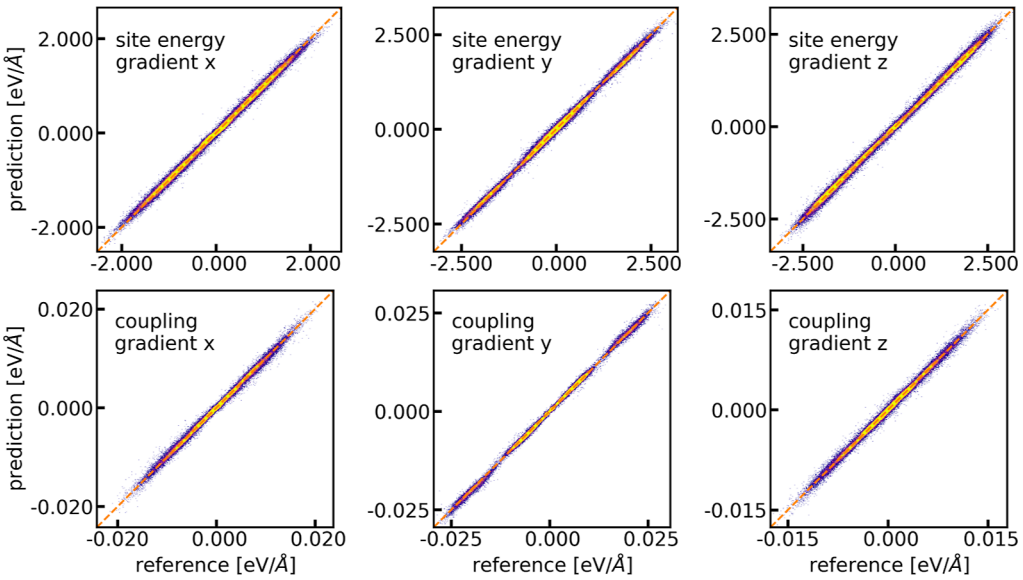

Figure 6. Scattering plots of the NN-predicted excitonic site energy gradient components (top) and TrMull coupling gradient component (bottom) of the ANT *b*-direction.

Table 4. Exciton Coupling and Reorganization Energy [meV] of ANT, PEN, PDI, and DIP in Different Crystallographic Directions[a]

	dir	dist.	$\langle V^{\text{Coulomb}}_{\text{TD-LCDFTB2}} \rangle$	$\langle V^{\text{TrMull}}_{\text{NN}} \rangle$	$\langle \lambda_{\text{NN}} \rangle$	$\lambda_{\text{TD-LCDFTB2}}$
ANT	*a*	5.24	6 ± 8	6 ± 6	493	494
	b	6.04	−27 ± 5	−27 ± 4		
PEN	*p*	6.24	−27 ± 6	−27 ± 4	330	329
	t_1	4.69	−10 ± 7	−10 ± 6		
	t_2	5.16	−9 ± 7	−9 ± 6		
PDI	*p*	4.86	82 ± 12	79 ± 7	352	367
	t_1	9.40	−32 ± 3	−29 ± 2		
	t_2	11.60	−15 ± 6	−14 ± 3		
	t_3	15.10	14 ± 4	12 ± 2		
DIP	*a*	7.17	59 ± 9	59 ± 7	378	378
	b	5.58	−85 ± 7	−84 ± 6		

[a]Dist. is in Å. ⟨ ⟩ indicates the average values of the properties during a course of MD simulation.

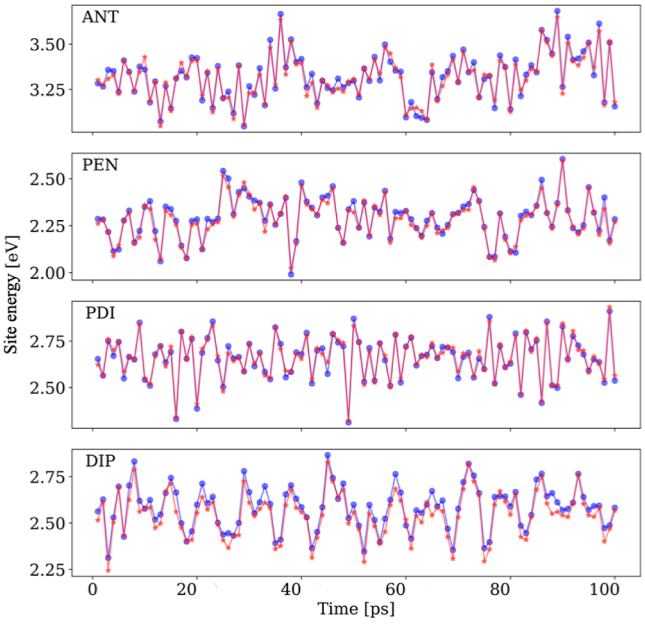

Figure 7. Time evolution of exciton site energies. Site energies were calculated with LC-DFTB2 (red) and NN models (blue) in the same trajectories.

tions play a beneficial role in aiding the localized exciton to surmount activation barriers.

3.5. Exciton Propagation Using Trajectory Surface Hopping. Table 5 shows the diffusion constants and averaged inverse participation ratios (IPR, eq 16) computed by the FSSH (ER) and BC-FSSH-IR methods, as discussed in the Methods section. Experimental data for the diffusion constants are available only for anthracene (ANT). The computed value in the ANT *b*-direction of 2.2 × 10^{-3} cm^2 s^{-1} is close to experimental value and agrees with the theoretical estimate by Giannini et al.[26] (see Table 5). The diffusion constants obtained from our simulations slightly underestimate the experimental values. This discrepancy, also found in previous work,[19] can be attributed to the neglect of nuclear zero-point energies which can have an impact when dealing with substantial activation barriers, as discussed also for charge-transfer processes in ref 45.

Beyond anthracene, we investigated other relevant organic semiconductors, including PDI, DIP, and PEN. It must be noted that, in experiment, singlet-excited pentacene relaxes to two triplets via singlet fission within 100 fs;[72] therefore, the singlet diffusion constant is only of theoretical interest. While for anthracene a clear hopping-type transfer mechanism is found, as detailed in our previous work,[19] the delocalization of the exciton wave function as measured by ⟨IPR⟩ is larger for some other materials like PDI *p*-direction and DIP *b*-direction, which indicates the transition delocalization transport mechanism.[26] In the DIP *b*-direction, the exciton coupling (−84 meV) and reorganization energy (378 meV) closely resemble those in PDI, see Table 4, yet the exciton wave function exhibits less delocalization, as inferred from the ⟨IPR⟩ values in Table 5. Consequently, the diffusion constant in DIP is lower. In contrast, the PEN *p*-direction, with an exciton coupling identical to that in ANT *b*-direction but a reorganization

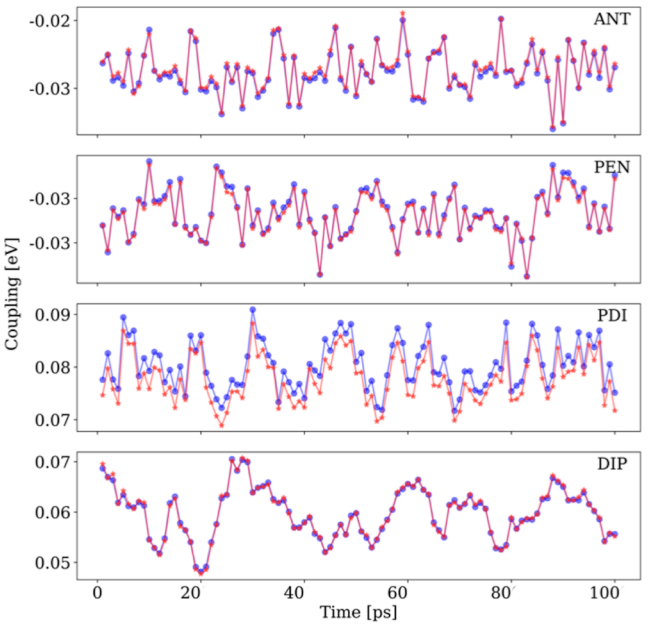

Figure 8. Time evolution of exciton coupling. Exciton couplings were calculated with LC-DFTB2 (red) and NN models (blue) in the same trajectories.

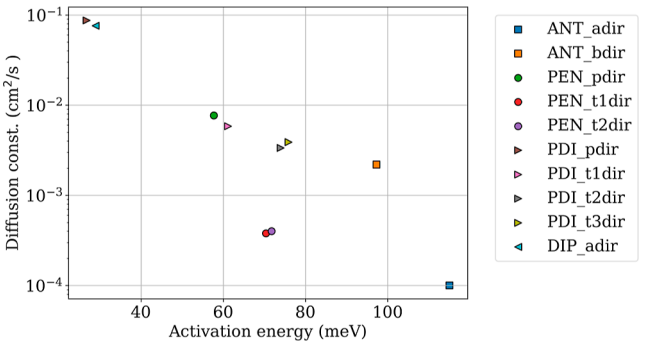

Figure 9. Exciton diffusion constant (cm^2/s) of ANT, PEN, PDI, and DIP in different crystallographic directions vs activation barrier (in meV).

energy 33 meV lower, demonstrates a diffusion constant more than threefold higher than that in ANT *b*-direction and slightly higher delocalization, underscoring the consistency and reliability of our results.

Here, a notable trend is observed where lower reorganization energies, relative to excitonic coupling values, lead to higher diffusion constants in excitonic systems, accompanied by a larger delocalization. This relation has been widely studied for charge transfer, as discussed in Introduction, but has been systematically examined for exciton transfer only recently by Giannini et al.[26] The authors discussed the different performances of the materials studied in their work in terms of barrier heights associated with hypothetical site-to-site transfer of exciton, eq 17, under the framework of the two-state harmonic approximation.

$$\Delta A^{\ddagger} = \frac{\lambda}{4} - \langle |V_{ij}|^2 \rangle^{1/2} + \frac{1}{\lambda}\langle |V_{ij}|^2 \rangle \qquad (17)$$

In this formula, V corresponds to the coupling elements. The variable λ denotes the reorganization energy relevant to the exciton transfer. Notably, when coupling values are substantial, the barrier shifts from being an impediment to forming a minimum. Similar to the study of Giannini et al., we find a relation between barrier height, as given by the two parameters V and λ, and diffusion constants as shown in Figure 9 for the specific crystallographic directions. The diffusion constants increase almost linearly with the decrease of barrier heights, and this finding aligns well with that of Giannini et al., and our study adds one more promising candidate for high diffusion constants (DIP), as indicated already by recent experiments.[73]

The agreement with experimental results and in particular with the alternative theoretical approach of Giannini et al.[26] demonstrates the reliability and robustness of complex multiscale methods to predict relevant observables for OSCs. While agreeing on the overall picture, there are differences in details.

Our diffusion constant for PDI in the *p*-direction is about 3 times as high as that reported by Giannini et al.[26] In the Marcus theory, the reorganization energy is logarithmically related to the transfer rate constant, which seems to be approximately preserved in our simulations, since we find a linear relation of barrier heights and logarithm of the diffusion constant. Therefore, there is a very high sensitivity with respect to the parameters of the simulation, which slightly differ

Table 5. Diffusion Constant D ($\times 10^{-3}$ cm^2 s^{-1}) and Averaged Wave Function Delocalization ($\langle IPR \rangle$) Value of ANT, PEN, PDI, and DIP in Different Crystallographic Directions Using ER and Boltzmann-Corrected IR FSSH Algorithm

		FSSH		BC-FSSH-IR		ref.	
crystals	directions	D_{ER}	$\langle IPR \rangle_{ER}$	D_{IR}	$\langle IPR \rangle_{IR}$	D_{com}[a]	D_{exp}
ANT	*a*	0.1	1.0	0.4	1.0	0.5[b,19] 0.8[c26]	1.8[71]
	b	2.2	1.0	8.2	1.0	2.4[b,26] 3.3[c26]	5.1[71]
PEN	*p*	7.7	1.1	25.2	1.1		
	t_1	0.4	1.0	1.1	1.0		
	t_2	0.4	1.0	1.1	1.0		
PDI	*p*	87.2	1.7	158.2	1.7	26.0[c26]	
	t_1	5.8	1.1	17.5	1.1		
	t_2	3.4	1.0	7.7	1.0		
	t_3	3.9	1.0	3.3	1.0		
DIP	*b*	76.1	1.4	146.2	1.6		

[a] D_{com} is the computed exciton diffusion constant. [b] Exciton diffusion constant obtained from the 1D modeling of the exciton transfer. [c] Exciton diffusion constant obtained from the 2D modeling of the exciton transfer.

between the different approaches. As shown in Table 3, there is some uncertainty regarding the reorganization energies; LC-DFT approaches gives slightly higher values than SCS-CC2, while LC-DFTB2 underestimates this value compared to the reference value. In the case of PDI, the NNs even predict a slightly lower value of 352 meV (Table 4), which has to be compared to the value of 388 meV at the CAM-B3LYP level as used by Giannini et al.[26]

In this regard, we computed the diffusion constant in the PDI *p*-direction with IR-BC-FSSH approximation, with the reorganization energy predicted by NN, 352 meV, and the reorganization energy obtained from the four-point calculation via DFT/CAM-B3LYP, 388 meV (Table 3). The results show a reduction of almost 0.040 $cm^2\ s^{-1}$ in diffusion constant as the diffusion constant calculated by IR-BC-FSSH and the NN reorganization energy is 0.158 $cm^2\ s^{-1}$, while the diffusion constant calculated by the IR-BC-FSSH and DFT/CAM-B3LYP reorganization energy is 0.120 $cm^2\ s^{-1}$. Applying the same strategy for ANT *b*-direction also indicates more than 50% reduction in the diffusion constant as the diffusion constant calculated by IR-BC-FSSH and NN reorganization energy, 494 meV, is 0.0081 $cm^2\ s^{-1}$ and the diffusion constant calculated by IR-BC-FSSH and DFT/ωB97XD reorganization energy, 562 meV, is 0.0031 $cm^2\ s^{-1}$.

The couplings agree quite well between the two methods; for PDI, we find a slightly lower averaged value of 79 meV compared to the value of 105 meV reported by Giannini et al. for PDI in the *p*-direction. While this reduced exciton coupling also affects the diffusion constant, its influence is overshadowed by the implications of the higher reorganization energy.

Therefore, there is a range of parameter values that define the error bars of the multiscale simulations. Despite this uncertainty, it should be noted that the predictions have a fair accuracy, since the qualitative features are predicted very well, and predictions within the chemical accuracy (1 kcal/mol) of barrier heights translate into an uncertainty of about 0.043 eV. This value marks the expected variation within the theoretical results, and the difference in parameters between our method and that of Giannini et al.[26] is within this range.

Besides parametrization, there are also a few methodological differences, which could play out at that energy scale: (i) while Giannini et al. consider long-range exciton coupling effects, we consider strictly first-neighbor exciton couplings. The latter may lead to a larger delocalization of the exciton wave function and, consequently, a higher exciton diffusion constant. This may contribute to the difference in the IPR values, with ours being 1.7 compared to their 1.4.[26] (ii) Second, differences may arise from the distinct modifications applied to the force field to reproduce energies and forces. Our NN is trained w.r.t. LC-TD-DFTB energies and forces, which include anharmonicity for both ground- and excited-state properties, whereas Giannini et al. parametrized bonding parameters based on excited-state data to align with DFT-calculated reorganization energies. This may result in a slightly different representation of fluctuations. (iii) Third, we only considered 1D QM zones, consisting of a row of molecules selected from a specific crystallographic direction, while Giannini et al.[26] mostly considered 2D simulation of the exciton transfer. Considering 1D exciton transfer in crystals where there is an isotropy of exciton coupling in all directions leads to the underestimation of the diffusion constant. This can also lead to overestimation of anisotropy in diffusion constants within a plane as for ANT a- and *b*-directions in Table 5. In 2D, dynamics in one direction (*b*-direction) can "help" overcome barriers in the other direction (*a*-direction).

We extended our investigation by calculating the diffusion constants in the PDI *p*-direction and ANT *b*-direction, with the IR-BC-FSSH approximation employing constant values of the couplings. Using the DFT/CAM-B3LYP reorganization energy of 388 and 105 meV as the constant coupling value for the PDI *p*-direction results in a diffusion constant of 0.168 $cm^2\ s^{-1}$, which is almost 0.050 $cm^2\ s^{-1}$ higher than the case for fluctuating couplings, which results in 0.120 $cm^2\ s^{-1}$. In ANT *b*-direction, using the DFT/ωB97XD reorganization energy of 562 meV and constant coupling of −29.5 meV, from ref 26, leads to a diffusion constant of 0.005 $cm^2\ s^{-1}$, which is increased compared to the simulation with fluctuating couplings, where the diffusion constant is 0.003 $cm^2\ s^{-1}$. It must be noted that the average coupling for the simulation with fluctuating couplings is −25 meV.

We also evaluated an approximation to the FSSH method using an IR and Boltzmann correction scheme (IR-BC-FSSH), which has been very valuable in the case of charge transfer.[39,45] Notably, the results from IR-BC-FSSH consistently overestimate the diffusion constant compared to the standard FSSH across all cases. This overestimation is attributed to the instantaneous relaxation assumption inherent in the IR-BC-FSSH method, as previously observed in our charge-transfer studies.[45] The value of this approach is that the effect of reorganization energy can be estimated directly, as shown above.

Calculating the site energy of a single anthracene molecule using TD-LC-DFTB2 in the gas phase requires approximately 1.02 s on Intel(R) Xeon(R) Gold 6226R CPU @ 2.90 GHz. In contrast, employing a neural network (NN) significantly reduces this computation time to just 67 μs on Intel(R) Xeon(R) CPU E5-2630 v2 @ 2.60 GHz. This substantial improvement illustrates the remarkable computational efficiency by nearly a factor of 20,000 for the NN approach.

4. CONCLUSIONS

In this work, we have developed a multiscale simulation methodology specifically tailored for the propagation of Frenkel singlet excitons in OSC crystals. Our approach incorporates neural network models designed to accurately predict critical parameters such as site energies, excitonic couplings, and their derivatives. These parameters are integral to the successful implementation of the nonadiabatic molecular dynamics simulation framework. Utilizing the FSSH algorithm, the method allows the study of exciton dynamics for complex models of OSCs.

A cornerstone of our methodology is the generation of high-fidelity data necessary for effective training of our neural networks. For this, we employed the long-range correction version of the time-dependent density functional tight-binding with self-consistent charges (TD-LC-DFTB2)method. As shown above, the site energies, Coulomb couplings, and reorganization energies calculated with TD-LC-DFTB2align very well with those obtained from the more expensive long range TD-DFT and CC2. This is remarkable since the efficiency of LC-DFTB allows us to generate a sufficient amount of training data at a very low cost.

We applied this methodology to four OSC crystals: ANT, PEN, PDI, and DIP. The results agree reasonably not only with experimental data but also with the theoretical data

obtained by simular multiscale method used by Giannini et al. This is encouraging, since the two methods are complicated multiscale methods based on similar, but not identical, computational protocols.

Our study demonstrates the potential of our multiscale method to simulate exciton propagation in OSCs. By combining neural network models with the FSSH algorithm, we can gain valuable insights into the exciton diffusion dynamics in these materials. Moreover, the incorporation of neural network models and efficient quantum chemical approaches like LC-DFTB for generating the training data enable us to construct a fast and reliable model, which would potentially aid in the optimization of materials for organic electronics.

AUTHOR INFORMATION

Corresponding Author

Weiwei Xie − *Frontiers Science Center for New Organic Matter, Key Laboratory of Advanced Energy Materials Chemistry (Ministry of Education), State Key Laboratory of Advanced Chemical Power Sources, College of Chemistry, Nankai University, Tianjin 300071, China;* orcid.org/0000-0001-8224-5340; Email: xieweiwei@nankai.edu.cn

Authors

Farhad Ghalami − *Institute of Physical Chemistry (IPC), Karlsruhe Institute of Technology, 76131 Karlsruhe, Germany; Institute of Nano Technology (INT), Karlsruhe Institute of Technology, 76344 Eggenstein-Leopoldshafen, Germany*

Philipp M. Dohmen − *Institute of Physical Chemistry (IPC), Karlsruhe Institute of Technology, 76131 Karlsruhe, Germany*

Mila Krämer − *Institute of Physical Chemistry (IPC), Karlsruhe Institute of Technology, 76131 Karlsruhe, Germany*

Marcus Elstner − *Institute of Physical Chemistry (IPC), Karlsruhe Institute of Technology, 76131 Karlsruhe, Germany; Institute of Nano Technology (INT), Karlsruhe Institute of Technology, 76344 Eggenstein-Leopoldshafen, Germany; Institute of Biological Interfaces (IBG-2), Karlsruhe Institute of Technology, 76131 Karlsruhe, Germany;* orcid.org/0000-0002-3255-306X

Notes

The authors declare no competing financial interest.

ACKNOWLEDGMENTS

This work has been supported by the Deutsche Forschungsgemeinschaft (DFG) through SFB 1249 "N-Heteropolycycles as Functional Materials" (Project B02). The authors acknowledge support by the state of Baden-Württemberg through bwHPC and the German Research Foundation (DFG) through grant no INST 40/575-1 FUGG (JUSTUS 2 cluster). W.X. is thankful for the financial support from the National Natural Science Foundation of China (no. 22203047). The authors acknowledge financial support from the Klaus Tschira Foundation through SIMPLAIX. They gratefully acknowledge the support by the German Research Foundation (DFG) through the Research Training Group 2450.

REFERENCES

(1) Dimitriev, O. P. Dynamics of excitons in conjugated molecules and organic semiconductor systems. *Chem. Rev.* **2022**, *122*, 8487−8593.

(2) Armstrong, N. R.; Wang, W.; Alloway, D. M.; Placencia, D.; Ratcliff, E.; Brumbach, M. Organic/organic heterojunctions: organic light emitting diodes and organic photovoltaic devices. *Macromol. Rapid Commun.* **2009**, *30*, 717−731.

(3) Meerheim, R.; Lussem, B.; Leo, K. Efficiency and stability of pin type organic light emitting diodes for display and lighting applications. *Proc. IEEE* **2009**, *97*, 1606−1626.

(4) Kulkarni, A. P.; Tonzola, C. J.; Babel, A.; Jenekhe, S. A. Electron transport materials for organic light-emitting diodes. *Chem. Mater.* **2004**, *16*, 4556−4573.

(5) Dimitrakopoulos, C. D.; Malenfant, P. R. Organic thin film transistors for large area electronics. *Adv. Mater.* **2002**, *14*, 99−117.

(6) Newman, C. R.; Frisbie, C. D.; da Silva Filho, D. A.; Brédas, J. L.; Ewbank, P. C.; Mann, K. R. Introduction to organic thin film transistors and design of n-channel organic semiconductors. *Chem. Mater.* **2004**, *16*, 4436−4451.

(7) Kippelen, B.; Brédas, J. L. Organic photovoltaics. *Energy Environ. Sci.* **2009**, *2*, 251−261.

(8) Dennler, G.; Scharber, M. C.; Brabec, C. J. Polymer-fullerene bulk-heterojunction solar cells. *Adv. Mater.* **2009**, *21*, 1323−1338.

(9) Li, S.; Li, Z.; Wan, X.; Chen, Y. Recent progress in flexible organic solar cells. *eScience* **2023**, *3*, 100085.

(10) Lu, Y.; Chen, J. Prospects of organic electrode materials for practical lithium batteries. *Nat. Rev. Chem* **2020**, *4*, 127−142.

(11) Cao, S.; Zhang, H.; Zhao, Y.; Zhao, Y. Pillararene/Calixarene-based systems for battery and supercapacitor applications. *EScience* **2021**, *1*, 28−43.

(12) Birkmeier, K.; Hertel, T.; Hartschuh, A. Probing the ultrafast dynamics of excitons in single semiconducting carbon nanotubes. *Nat. Commun.* **2022**, *13*, 6290.

(13) Sharma, A.; Hasan, M. M.; Lu, Y. Exciton dynamics in 2D organic semiconductors. *Mater. Futures* **2022**, *1*, 042001.

(14) Ostroverkhova, O. Organic Optoelectronic Materials: Mechanisms and Applications. *Chem. Rev.* **2016**, *116*, 13279−13412.

(15) Müller, K.; Schellhammer, K. S.; Gräßler, N.; Debnath, B.; Liu, F.; Krupskaya, Y.; Leo, K.; Knupfer, M.; Ortmann, F. Directed exciton transport highways in organic semiconductors. *Nat. Commun.* **2023**, *14*, 5599.

(16) Omar, Ö. H.; Del Cueto, M.; Nematiaram, T.; Troisi, A. High-throughput virtual screening for organic electronics: a comparative study of alternative strategies. *J. Mater. Chem. C* **2021**, *9*, 13557−13583.

(17) Stehr, V.; Engels, B.; Deibel, C.; Fink, R. Anisotropy of singlet exciton diffusion in organic semiconductor crystals from ab initio approaches. *J. Chem. Phys.* **2014**, *140*, 024503.

(18) Stehr, V.; Fink, R. F.; Deibel, C.; Engels, B. Charge carrier mobilities in organic semiconductor crystals based on the spectral overlap. *J. Comput. Chem.* **2016**, *37*, 2146−2156.

(19) Kranz, J. J.; Elstner, M. Simulation of singlet exciton diffusion in bulk organic materials. *J. Chem. Theory Comput.* **2016**, *12*, 4209−4221.
(20) Heck, A.; Kranz, J. J.; Kubar, T.; Elstner, M. Multi-scale approach to non-adiabatic charge transport in high-mobility organic semiconductors. *J. Chem. Theory Comput.* **2015**, *11*, 5068−5082.
(21) Heck, A.; Kranz, J. J.; Elstner, M. Simulation of temperature-dependent charge transport in organic semiconductors with various degrees of disorder. *J. Chem. Theory Comput.* **2016**, *12*, 3087−3096.
(22) Sala, M.; Guérin, S.; Gatti, F. Quantum dynamics of the photostability of pyrazine. *Phys. Chem. Chem. Phys.* **2015**, *17*, 29518−29530.
(23) Xie, W.; Holub, D.; Kubař, T.; Elstner, M. Performance of Mixed Quantum-Classical Approaches on Modeling the Crossover from Hopping to Bandlike Charge Transport in Organic Semiconductors. *J. Chem. Theory Comput.* **2020**, *16*, 2071−2084.
(24) Oberhofer, H.; Reuter, K.; Blumberger, J. Charge transport in molecular materials: An assessment of computational methods. *Chem. Rev.* **2017**, *117*, 10319−10357.
(25) Giannini, S.; Blumberger, J. Charge transport in organic semiconductors: the perspective from nonadiabatic molecular dynamics. *Acc. Chem. Res.* **2022**, *55*, 819−830.
(26) Giannini, S.; Peng, W.-T.; Cupellini, L.; Padula, D.; Carof, A.; Blumberger, J. Exciton transport in molecular organic semiconductors boosted by transient quantum delocalization. *Nat. Commun.* **2022**, *13*, 2755.
(27) Brey, D.; Burghardt, I. Coherent Transient Localization Mechanism of Interchain Exciton Transport in Regioregular P3HT: A Quantum-Dynamical Study. *J. Phys. Chem. Lett.* **2024**, *15*, 1836−1845.
(28) Toldo, J. M.; Do Casal, M. T.; Ventura, E.; Do Monte, S. A.; Barbatti, M. Surface hopping modeling of charge and energy transfer in active environments. *Phys. Chem. Chem. Phys.* **2023**, *25*, 8293−8316.
(29) Peng, W.-T.; Brey, D.; Giannini, S.; Dell'Angelo, D.; Burghardt, I.; Blumberger, J. Exciton dissociation in a model organic interface: Excitonic state-based surface hopping versus multiconfigurational time-dependent Hartree. *J. Phys. Chem. Lett.* **2022**, *13*, 7105−7112.
(30) Fratini, S.; Ciuchi, S.; Mayou, D.; de Laissardière, G. T.; Troisi, A. A map of high-mobility molecular semiconductors. *Nat. Mater.* **2017**, *16*, 998−1002.
(31) Ciuchi, S.; Fratini, S.; Mayou, D. Transient localization in crystalline organic semiconductors. *Phys. Rev. B* **2011**, *83*, 081202.
(32) Nematiaram, T.; Ciuchi, S.; Xie, X.; Fratini, S.; Troisi, A. Practical computation of the charge mobility in molecular semiconductors using transient localization theory. *J. Phys. Chem. C* **2019**, *123*, 6989−6997.
(33) Alvertis, A. M.; Haber, J. B.; Engel, E. A.; Sharifzadeh, S.; Neaton, J. B. Phonon-induced localization of excitons in molecular crystals from First Principles. *Phys. Rev. Lett.* **2023**, *130*, 086401.
(34) Stojanović, L.; Coker, J.; Giannini, S.; Londi, G.; Gertsen, A. S.; Wenzel Andreasen, J.; Yan, J.; D'Avino, G.; Beljonne, D.; Nelson, J.; et al. Disorder-Induced Transition from Transient Quantum Delocalization to Charge Carrier Hopping Conduction in a Nonfullerene Acceptor Material. *Phys. Rev. X* **2024**, *14*, 021021.
(35) Sneyd, A. J.; Beljonne, D.; Rao, A. A new frontier in exciton transport: transient delocalization. *J. Phys. Chem. Lett.* **2022**, *13*, 6820−6830.
(36) Bold, B. M.; Sokolov, M.; Maity, S.; Wanko, M.; Dohmen, P. M.; Kranz, J. J.; Kleinekathöfer, U.; Höfener, S.; Elstner, M. Benchmark and performance of long-range corrected time-dependent density functional tight binding (LC-TD-DFTB) on rhodopsins and light-harvesting complexes. *Phys. Chem. Chem. Phys.* **2020**, *22*, 10500−10518.
(37) Sokolov, M.; Bold, B. M.; Kranz, J. J.; Höfener, S.; Niehaus, T. A.; Elstner, M. Analytical Time-Dependent Long-Range Corrected Density Functional Tight Binding (TD-LC-DFTB) Gradients in DFTB+: Implementation and Benchmark for Excited-State Geometries and Transition Energies. *J. Chem. Theory Comput.* **2021**, *17*, 2266−2282.
(38) Schieschke, N.; Bold, B. M.; Dohmen, P. M.; Wehl, D.; Hoffmann, M.; Dreuw, A.; Elstner, M.; Höfener, S. Geometry dependence of excitonic couplings and the consequences for configuration-space sampling. *J. Comput. Chem.* **2021**, *42*, 1402−1418.
(39) Dohmen, P. M.; Krämer, M.; Reiser, P.; Friederich, P.; Elstner, M.; Xie, W. Modeling Charge Transport in Organic Semiconductors Using Neural Network Based Hamiltonians and Forces. *J. Chem. Theory Comput.* **2023**, *19*, 3825−3838.
(40) Kubar, T.; Elstner, M. Coarse-grained time-dependent density functional simulation of charge transfer in complex systems: application to hole transfer in DNA. *J. Phys. Chem. B* **2010**, *114*, 11221−11240.
(41) Lüdemann, G.; Woiczikowski, P. B.; Kubar, T.; Elstner, M.; Steinbrecher, T. B. Charge transfer in E. coli DNA photolyase: Understanding polarization and stabilization effects via QM/MM simulations. *J. Phys. Chem. B* **2013**, *117*, 10769−10778.
(42) Lüdemann, G.; Solov'yov, I. A.; Kubař, T.; Elstner, M. Solvent driving force ensures fast formation of a persistent and well-separated radical pair in plant cryptochrome. *J. Am. Chem. Soc.* **2015**, *137*, 1147−1156.
(43) Haldar, R.; Kozlowska, M.; Ganschow, M.; Ghosh, S.; Jakoby, M.; Chen, H.; Ghalami, F.; Xie, W.; Heidrich, S.; Tsutsui, Y.; et al. Interplay of structural dynamics and electronic effects in an engineered assembly of pentacene in a metal−organic framework. *Chem. Sci.* **2021**, *12*, 4477−4483.
(44) Krämer, M.; Dohmen, P. M.; Xie, W.; Holub, D.; Christensen, A. S.; Elstner, M. Charge and exciton transfer simulations using machine-learned Hamiltonians. *J. Chem. Theory Comput.* **2020**, *16*, 4061−4070.
(45) Roosta, S.; Ghalami, F.; Elstner, M.; Xie, W. Efficient surface hopping approach for modeling charge transport in organic semiconductors. *J. Chem. Theory Comput.* **2022**, *18*, 1264−1274.
(46) Senn, H. M.; Thiel, W. QM/MM methods for biomolecular systems. *Angew. Chem., Int. Ed.* **2009**, *48*, 1198−1229.
(47) Plötz, P. A.; Niehaus, T.; Kühn, O. A new efficient method for calculation of Frenkel exciton parameters in molecular aggregates. *J. Chem. Phys.* **2014**, *140*, 174101.
(48) Spencer, J.; Gajdos, F.; Blumberger, J. FOB-SH: Fragment orbital-based surface hopping for charge carrier transport in organic and biological molecules and materials. *J. Chem. Phys.* **2016**, *145*, 064102.
(49) Carof, A.; Giannini, S.; Blumberger, J. Detailed balance, internal consistency, and energy conservation in fragment orbital-based surface hopping. *J. Chem. Phys.* **2017**, *147*, 214113.
(50) Li, J.; Reiser, P.; Boswell, B. R.; Eberhard, A.; Burns, N. Z.; Friederich, P.; Lopez, S. A. Automatic discovery of photoisomerization mechanisms with nanosecond machine learning photodynamics simulations. *Chem. Sci.* **2021**, *12*, 5302−5314.
(51) Kranz, J. J.; Elstner, M.; Aradi, B.; Frauenheim, T.; Lutsker, V.; Garcia, A. D.; Niehaus, T. A. Time-dependent extension of the long-range corrected density functional based tight-binding method. *J. Chem. Theory Comput.* **2017**, *13*, 1737−1747.
(52) Vuong, V. Q.; Akkarapattiakal Kuriappan, J.; Kubillus, M.; Kranz, J. J.; Mast, T.; Niehaus, T. A.; Irle, S.; Elstner, M. Parametrization and benchmark of long-range corrected DFTB2 for organic molecules. *J. Chem. Theory Comput.* **2018**, *14*, 115−125.
(53) Frisch, M. J.; Trucks, G. W.; Schlegel, H. B.; Scuseria, G. E.; Robb, M. A.; Cheeseman, J. R.; Scalmani, G.; Barone, V.; Petersson, G. A.; Nakatsuji, H.; Li, X.; Caricato, M.; Marenich, A. V.; Bloino, J.; Janesko, B. G.; Gomperts, R.; Mennucci, B.; Hratchian, H. P.; Ortiz, J. V.; Izmaylov, A. F.; Sonnenberg, J. L.; Williams-Young, D.; Ding, F.; Lipparini, F.; Egidi, F.; Goings, J.; Peng, B.; Petrone, A.; Henderson, T.; Ranasinghe, D.; Zakrzewski, V. G.; Gao, J.; Rega, N.; Zheng, G.; Liang, W.; Hada, M.; Ehara, M.; Toyota, K.; Fukuda, R.; Hasegawa, J.; Ishida, M.; Nakajima, T.; Honda, Y.; Kitao, O.; Nakai, H.; Vreven, T.; Throssell, K.; Montgomery Jr, J. A.; Peralta, J. E.; Ogliaro, F.; Bearpark, M. J.; Heyd, J. J.; Brothers, E. N.; Kudin, K. N.; Staroverov,

V. N.; Keith, T. A.; Kobayashi, R.; Normand, J.; Raghavachari, K.; Rendell, A. P.; Burant, J. C.; Iyengar, S. S.; Tomasi, J.; Cossi, M.; Millam, J. M.; Klene, M.; Adamo, C.; Cammi, R.; Ochterski, J. W.; Martin, R. L.; Morokuma, K.; Farkas, O.; Foresman, J. B.; Fox, D. J. *Gaussian 16*. Revision C.01; Gaussian Inc.: Wallingford CT, 2016.
(54) Aradi, B.; Hourahine, B.; Frauenheim, T. *DFTB, a Versatile and Accurate Method for Efficient Quantum Mechanical Simulations*, 2008.
(55) Humeniuk, A.; Mitrić, R. Long-range correction for tight-binding TD-DFT. *J. Chem. Phys.* **2015**, *143*, 134120.
(56) Gaus, M.; Cui, Q.; Elstner, M. Density functional tight binding: application to organic and biological molecules. *Wiley Interdiscip. Rev.: Comput. Mol. Sci.* **2014**, *4*, 49−61.
(57) Klambauer, G.; Unterthiner, T.; Mayr, A.; Hochreiter, S. Self-normalizing neural networks. In *31st Conference on Neural Information Processing Systems (NIPS 2017)*: Long Beach, CA, USA, 2017, p 30.
(58) Abadi, M.; Agarwal, A.; Barham, P.; Brevdo, E.; Chen, Z.; Citro, C.; Corrado, G. S.; Davis, A.; Dean, J.; Devin, M.; et al. Tensorflow: Large-scale machine learning on heterogeneous distributed systems. *arXiv* **2016**, arXiv:1603.04467.
(59) Chollet, F.; et al. *Keras: the python Deep Learning Library*; Astrophysics source code library, 2018.
(60) Kingma, D. P.; Ba, J. Adam: A method for stochastic optimization. *arXiv* **2014**, arXiv:1412.6980.
(61) Li, L.; Jamieson, K.; DeSalvo, G.; Rostamizadeh, A.; Talwalkar, A. Hyperband: A novel bandit-based approach to hyperparameter optimization. *J. Mach. Learn. Res.* **2017**, *18*, 1−52.
(62) Wang, J.; Wolf, R. M.; Caldwell, J. W.; Kollman, P. A.; Case, D. A. Development and testing of a general amber force field. *J. Comput. Chem.* **2004**, *25*, 1157−1174.
(63) Wang, J.; Wang, W.; Kollman, P. A.; Case, D. A. Automatic atom type and bond type perception in molecular mechanical calculations. *J. Mol. Graph. Model.* **2006**, *25*, 247−260.
(64) Singh, U. C.; Kollman, P. A. An approach to computing electrostatic charges for molecules. *J. Comput. Chem.* **1984**, *5*, 129−145.
(65) Besler, B. H.; Merz, K. M.; Kollman, P. A. Atomic charges derived from semi-empirical methods. *J. Comput. Chem.* **1990**, *11*, 431−439.
(66) Evans, D. J.; Holian, B. L. The Nose−Hoover thermostat. *J. Chem. Phys.* **1985**, *83*, 4069−4074.
(67) Abraham, M. J.; Murtola, T.; Schulz, R.; Páll, S.; Smith, J. C.; Hess, B.; Lindahl, E. GROMACS: High performance molecular simulations through multi-level parallelism from laptops to supercomputers. *SoftwareX* **2015**, *1−2*, 19−25.
(68) Aragó, J.; Sancho-García, J. C.; Ortí, E.; Beljonne, D. Ab Initio Modeling of Donor−Acceptor Interactions and Charge-Transfer Excitations in Molecular Complexes: The Case of Terthiophene−Tetracyanoquinodimethane. *J. Chem. Theory Comput.* **2011**, *7*, 2068−2077.
(69) Stehr, V.; Fink, R. F.; Tafipolski, M.; Deibel, C.; Engels, B. Comparison of different rate constant expressions for the prediction of charge and energy transport in oligoacenes. *Wiley Interdiscip. Rev. Comput. Mol. Sci.* **2016**, *6*, 694−720.
(70) Stehr, V.; Fink, R. F.; Engels, B.; Pflaum, J.; Deibel, C. Singlet exciton diffusion in organic crystals based on Marcus transfer rates. *J. Chem. Theory Comput.* **2014**, *10*, 1242−1255.
(71) Aragó, J.; Troisi, A. Regimes of exciton transport in molecular crystals in the presence of dynamic disorder. *Adv. Funct. Mater.* **2016**, *26*, 2316−2325.
(72) Burdett, J. J.; Bardeen, C. J. The dynamics of singlet fission in crystalline tetracene and covalent analogs. *Acc. Chem. Res.* **2013**, *46*, 1312−1320.
(73) Wirsing, S.; Hänsel, M.; Belova, V.; Schreiber, F.; Broch, K.; Engels, B.; Tegeder, P. Excited-state dynamics in perylene-based organic semiconductor thin films: Theory meets experiment. *J. Phys. Chem. C* **2019**, *123*, 27561−27572.